Intersubject Variability of Foveal Cone Photoreceptor Density in Relation to Eye Length

Kaccie Y. Li, Pavan Tiruveedhula, and Austin Roorda

Purpose. Adaptive optics scanning laser ophthalmoscopy (AOSLO) under optimized wavefront correction allows for routine imaging of foveal cone photoreceptors. The intersubject variability of foveal cone density was measured and its relation to eye length evaluated.

Methods. AOSLO was used to image 18 healthy eyes with axial lengths from 22.86 to 28.31 mm. Ocular biometry and an eye model were used to estimate the retinal magnification factor. Individual cones in the AOSLO images were labeled, and the locations were used to generate topographic maps representing the spatial distribution of density. Representative retinal (cones/mm^2) and angular (cones/deg^2) cone densities at specific eccentricities were calculated from these maps.

Results. The entire foveal cone mosaic was resolved in four eyes, whereas the cones within 0.03 mm eccentricity remained unresolved in most eyes. The preferred retinal locus deviated significantly ($P < 0.001$) from the point of peak cone density for all except one individual. A significant decrease in retinal density ($P < 0.05$) with increasing axial length was observed at 0.30 mm eccentricity but not closer. Longer, more myopic eyes generally had higher angular density near the foveal center than the shorter eyes, but by 1°, this difference was nullified by retinal expansion, and so angular densities across all eyes were similar.

Conclusions. The AOSLO can resolve the smallest foveal cones in certain eyes. Although myopia causes retinal stretching in the fovea, its effect within the foveola is confounded by factors other than cone density that have high levels of intersubject variability. (*Invest Ophthalmol Vis Sci.* 2010;51:6858–6867) DOI:10.1167/iovs.10-5499

Myopia is most often due to elongation of the vitreous chamber rather than changes in the cornea and lens. This fact is supported by the strong correlations between axial length and refractive error reported in many studies to date.[1–9] Reported complications that have been associated with myopia include lower best corrected acuity,[1,2,4,10] reduced sensitivity,[11,12] slower and/or inaccurate accommodation,[5,13,14] and object aspect ratio misperception.[15] Retinal stretching may be a plausible explanation for some of these observations, since a longer eye would require the same number of photoreceptors in the retina to tile over a larger surface area, an idea supported by cone density measurements from 1 to 2 mm eccentricity.[3] Although it may seem natural to extrapolate such findings into the foveal center, a study based on experimentally induced myopia in marmosets has shown that the opposite occurs, as the longer, myopic eyes actually had significantly higher retinal cone density (cones/mm^2) than the emmetropic eyes.[16] Therefore, the fact that the most dramatic changes in cone density distribution occur in the fovea begs for a more rigorous treatment of the matter.

In studies in which eye length is an important variable, extra care must be taken when reporting cone density or spacing as a function of eccentricity, because eye length directly affects the conversion between angular and retinal units. For example, a recent study reported a decrease in retinal cone density with increasing axial length at 2° eccentricity.[7] Whether their measurements supported the retinal stretch hypothesis, however, remains unknown, because 2° eccentricity corresponded to retinal eccentricities of 0.56 and 0.72 mm away from the foveal center for the shortest and longest eyes included in that study. According to anatomic measurements provided by Curcio et al.,[17] cone density was approximately 34,000 and 24,000 cones/mm^2 at 0.56 and 0.73 mm eccentricity, respectively. In the extreme case in which retinal cone density as a function of retinal eccentricity is preserved during eye growth, one would still expect to find a difference of approximately 10,000 cones/mm^2, owing to how a particular angular eccentricity converts to different retinal eccentricities when eye lengths are not equal. For clarity, we present our results in both angular and retinal units and discuss the visual and anatomic implications associated with each approach.

Foveal cones are not easily accessible in the living human eye, due to their small size, in addition to having to view them through the aberrated optics of the eye. Earlier in vivo techniques were indirect but were successful nevertheless in obtaining estimates of foveal cone spacing that were in reasonable agreement with histologic data.[18–20] Nevertheless, myopia related changes in cone spacing have most frequently been inferred from acuity measurements, with the general conclusion being that corrected myopes either perform similarly or worse than emmetropes, even after accounting for the minifying effects of the refractive correction.[1,2,4,10,21,22] Since myopes generally have higher retinal magnification due to their eye length, a likely explanation became that myopes may have increased cone spacing due to retinal stretching. Alternatively, in studies in which refractive error was corrected using spectacles and contact lenses, performance may have been compromised by optical factors such as scatter or high order aberrations.[1,4] Optical complications are minimized when acuity is tested with grating patterns generated with laser interference.[2,23] Using this method, the level of myopia no longer seemed to affect resolution acuity at the fovea. However, the higher retinal magnification factor (RMF) afforded by a longer eye would predict that myopes should actually perform better

From the School of Optometry, University of California, Berkeley, California.

Supported by NIH Bioengineering Research Partnership Grant EY014375, the NSF (National Science Foundation) Science and Technology Center for Adaptive Optics managed by the University of California at Santa Cruz under cooperative agreement AST-9876783, an American Optometric Foundation William C. Ezell Fellowship, and an International Society for Optics and Photonics (SPIE) Scholarship.

Submitted for publication March 3, 2010; revised May 14, 2010; accepted July 16, 2010.

Disclosure: **K.Y. Li**, None; **P. Tiruveedhula**, None; **A. Roorda**, P

Corresponding author: Austin Roorda, University of California, Berkeley, School of Optometry, 485 Minor Hall, Berkeley, CA 94720-2020; aroorda@berkeley.edu.

than emmetropes if their retinal cone densities were similar. Therefore, results from these two studies still support the idea that foveal cones become more widely spaced as myopia progresses.[2,23]

Advances in adaptive optics (AO) technology for high resolution retinal imaging[24–26] allow for direct observation of individual cone photoreceptors in the living human retina, but imaging foveal cones remains a challenge. To our knowledge, the flood illuminated AO ophthalmoscope at the University of Rochester is the only system to date that has demonstrated the capability of resolving the entire foveal cone mosaic in normal eyes.[27,28] Whether this system is able to achieve this level of performance in a group of individuals with different degrees of myopia is not known. Imaging the smallest cones in the central fovea using an adaptive optics scanning laser ophthalmoscope (AOSLO) has not yet been demonstrated. The present work applies our latest generation AOSLO[29] to imaging the foveal cone mosaic and investigating the relationship between foveal cone density and axial length. This system's wavefront compensation capabilities have been improved for the purpose of resolving the smallest foveal cones. Refinements to calculations for estimating retinal feature size and cone density are also described.

Methods

This research adhered to the tenets of the Declaration of Helsinki; informed consent was obtained from all subjects after the nature and possible complications of the study protocol were explained. The experiments were approved by the University of California, Berkeley Committee for the Protection of Human Subjects. Eighteen eyes of 18 healthy subjects, between the ages of 23 and 43 years were used in the study (Table 1). A self-report questionnaire was part of the subject recruitment process to ensure that only persons with no signs of ocular health problems were included in the study. Subjects who had smaller natural pupil sizes (<6 mm diameter) were administered 2.5% phenylephrine and 1% tropicamide before imaging. Retinas were imaged from fixation to just beyond 1° eccentricity.

Table 1. Subjects

	Eye	Sex	Age (y)	Axial Length (mm)	Spherical Equivalent Refraction (D)	RMF (μm/deg)
1	OD	F	31	22.86	0	272.20
2*	OD	M	29	22.87	0.5	270.68
3	OD	F	31	23.40	−1.5	278.75
4	OS	M	42	23.50	0	280.47
5	OD	M	30	23.51	0	281.47
6†	OD	F	24	24.08	0	288.41
7*	OS	M	43	24.18	0	288.49
8	OD	F	38	24.48	0	298.59
9‡	OS	M	31	24.49	−0.75	298.61
10	OD	F	23	24.54	−3.5	298.98
11	OS	M	36	25.00	−2.5	305.06
12	OD	M	43	25.37	−2.25	310.81
13†	OD	F	23	25.61	−5.5	316.58
14†	OS	F	23	25.73	−5.25	320.07
15†	OD	F	25	26.85	−6.75	335.61
16	OD	M	24	27.05	−7.0	341.68
17‡	OD	M	34	27.46	−4.5	348.84
18	OD	M	23	28.31	−11.0	362.32

* No cycloplegia administered.

† Entire cone mosaic resolved.

‡ Inaccurate ACD measurement. The ACD from the Gullstrand model eye (3.585 mm) was used.

Retinal Imaging

The AOSLO[29,30] consists of an 840 nm low coherence light source, a Shack-Hartmann wavefront sensor, and a MEMS deformable mirror (140-actuator with 3.5 μm stroke; Boston Micromachines, Cambridge, MA). Wavefront compensation upgrades that were implemented include faster frame rates (up to 25 Hz), higher step resolution driver electronics (14-bit) and an optimized wavefront reconstructor.[31,32] The actual frame rate depends on the exposure and readout times of the wavefront sensor CCD, with the former empirically adjusted on the basis of the reflectivity of the retina. The default controller is a pure integrator and a reconstructor (**R**) that inverts the interaction matrix[33,34] (**H**) by using noise and wavefront covariance matrices (**N** and **C**) as priors[32,35–37]:

$$\mathbf{R} = -(\mathbf{H}^{\mathrm{T}}\mathbf{N}^{-1}\mathbf{H} + \mathbf{C}^{-1} + \mathbf{V}\mathbf{V}^{\mathrm{T}})^{-1}\,\mathbf{H}^{\mathrm{T}}\mathbf{N}^{-1} \quad (1)$$

The parameter **V** is a 140 × 3 matrix, the columns of which are the three unobservable, deformable mirror modes: piston, tip, and tilt. Their inclusion in the matrix inversion is necessary for closed loop stability, when this type of reconstructor is used.[32] All computations were implemented in ANSI C, to ensure that real-time requirements were met. Eye alignment to the optical path and head stabilization were achieved via a chin rest and temple supports mounted on a three-axis stage. Imaging around the foveal center was performed with the subject fixating on a small, blinking stimulus, typically a square (<0.1° diameter), generated by turning the laser on and off between frames at appropriate moments of each raster scan.[38] The scan field was approximately 0.9° × 0.9°. Since the fixation target is part of the acquired image, fixation locations are recorded to simultaneously track each subject's fixation pattern.[38] The average fixation location on the retina was defined as the preferred retinal locus (PRL).

Image Processing and Analysis

The acquired retinal videos were first manually reviewed frame-by-frame for poor quality frames that may result from several factors (i.e., inaccurate wavefront measurement and/or correction, blink, and tear film breakup). These frames were deleted before further postprocessing. Next, the videos were corrected for sinusoidal and eye motion artifacts so that the retinal features in each frame were aligned.[39,40] The co-registered frames were then averaged to produce single, high signal-to-noise images. These steps were repeated for each acquired video, and the resultant images were stitched together (Photoshop; Adobe Systems, Inc., Mountain View, CA) to create a larger montage image of the foveal cone mosaic.

We implemented custom software for identifying individual cones in the AO retinal images in C++ with calls to several MatLab (The MathWorks, Inc., Natick, MA) functions via the MatLab Runtime Compiler. The interface allows the user to manually select individual cones and/or specify a region of interest for automated identification.[24,41] A combination of both manual and automated methods was used for analyzing the cone mosaic at and near the foveal center, because the current version of the automated algorithm does not perform adequately near the foveal center where the cones are smaller and consequently have lower contrast.

Retinal Feature Size Estimation

The adjusted axial length method coined by Bennett et al.[42] is often used to estimate the RMF.[10,42,43] This method assumes that the retina and the eye's back focal plane coincide, which is not the case in myopia. Since visual angle is defined with respect to the nodal points of the eye, a more reasonable approach would be to locate the second nodal point and the resultant retinal image size subtended by the nodal ray. We specified a four surface model eye for each subject. The anterior radius of curvature of the cornea (r_1), anterior chamber depth (ACD), and axial length were measured with an ocular biometer (IOLMaster; Carl Zeiss Meditec, Jena, Germany). For the cornea, we chose a fixed thickness and refractive index of 0.535 mm and 1.38, respective-

ly.[44,45] The corneal thickness was subtracted from the measured ACD to obtain the anatomic ACD (distance from the posterior cornea to the anterior lens). The posterior radius of curvature of the cornea (r_2) was taken to be $0.8831r_1$.[46] The Gullstrand schematic eye was used to approximate lens thickness and refractive indices of the aqueous, lens, and vitreous.

The location of the secondary nodal point was estimated for each eye via a paraxial ray trace.[47] Once determined, retinal image size was related to visual angle by the equation:

$$I = \tan(1^\circ)(x - \overline{AN'})\theta \quad (2)$$

where I is retinal image size, x is axial length, $\overline{AN'}$ is the distance from the corneal apex to the eye's second nodal point, and θ is the visual angle.

Another magnification factor must be applied to equation 2 when wavefront correction is aided with trial lenses. For example, a negative powered lens placed in front of the eye decreases the AOSLO's scan angle so that the resultant retinal image size will be smaller. This magnification factor is given by the thin lens formula:

$$M = \frac{1}{1 - P(d + y)} \quad (3)$$

where P is the power of the trial lens, d is the spectacle vertex distance, and y is the distance from the corneal apex to the entrance pupil. A fixed value of 14 mm was used for d for all subjects. The location of the entrance pupil was estimated from the ACD and the corneal radii of curvatures (r_1 and r_2).

Cone Density Estimation

Computations for estimating cone density were performed in MatLab with the MatLab Image Processing Toolbox (IPT). The procedure used for estimating density from a list of x, y locations was adapted from several earlier studies in which a fixed sampling window with an approximate area of 1300 μm^2 was scanned across the image to compute the mean density at each sampled location.[17,28,41] With this window size, the peak cone density averaged across the reported normal eye data was approximately 201,000 cones/mm^2.[17,28] Because of relatively higher cone density gradients near the foveal center, a fixed window size results in erroneous density estimates, due to averaging over a variable number of cones at different locations. We addressed this problem by adopting an adaptive sampling window whereby the window size is adjusted to contain a constant number of cones instead. The constant was set to 150, which is approximately the expected number of cones in a 1300 μm^2 sampling window based on published peak density values.[27,28,48]

Cone density is often calculated by dividing the number of cones recorded by the sampling window area. This method assumes a uniform density distribution within the sampling window and will underestimate density if the sampling window overlaps regions of missing data (i.e., image border). These limitations have motivated the adoption of what is known as the Voronoi local density analysis.[49–51] Figure 1 illustrates several steps in this computation procedure. After identifying individual cones in an image (Fig. 1a), the resultant coordinates are used to construct a binary mosaic that is all 0's except at pixels corresponding to the cone centers. The nearest-neighbor distance calculations are applied to the resultant binary mosaic using the IPT function bwdist.m. Voronoi tiles (Fig. 1c) are generated from the resultant distance image (Fig. 1b), by using the watershed transform (watershed.m), and tiles containing pixels on the image border are removed. Finally, a raw density value is calculated at each cone location by inverting the area of the corresponding Voronoi tile:

$$d(x,y) = \frac{1}{A[T(x,y)] + 0.5P[T(x,y)]} \quad (4)$$

where $A[T(x,y)]$ and $P[T(x,y)]$ are the area and perimeter of the Voronoi tile $T(x,y)$. Inclusion of the perimeter adjusts for the single pixel wide boundary that separates all adjacent Voronoi tiles. Raw density values of $d(x,y)$ were first scaled by the calibrated imaging field size to obtain angular density (cones/deg^2) and then once more with the appropriate RMF to obtain the retinal density (cones/mm^2). The cone density value reported at each particular cone location is taken as the mean of the local density estimates within its associated sampling window.

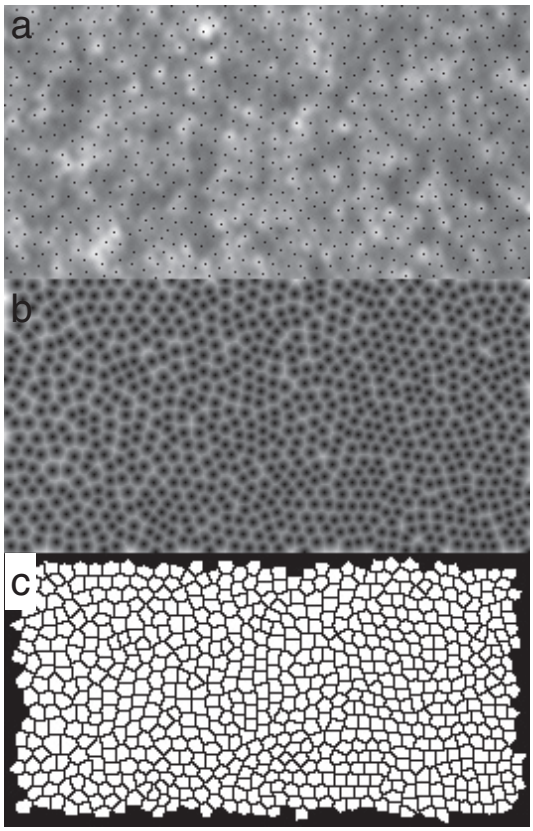

Figure 1. (**a**) A 0.25° × 0.50° (72 × 144 μm) section of a cone mosaic in subject 6 with identified cone locations. The patch is located at approximately 0.75° (216 μm) from the foveal center. (**b**) Result after taking the distance transform of the (x, y) cone locations. (**c**) Voronoi tiles generated using the watershed transform.

We defined the foveal center as the location of peak cone density. The two-dimensional sequence $d(x,y)$ was linearly interpolated to generate a cone-density topographic map for each eye. The location of peak cone density was determined from each topographic map by a center of mass calculation: average of the centroid locations for regions enclosed by the first six isodensity contour lines (contour levels are separated by 5000 cones/mm^2).[27,28] This method was adopted because it provides a systematic approach for estimating the peak density location when it is obviously located within the region where the cones were not resolved. This method was also applied to images without such a region, because errors due to cone mislabeling and digital artifacts can produce spikelike protrusions with artificially high values anywhere across the topographic map. Representative cone density measurements at particular eccentricities were computed by circular averaging of density estimates around all meridians. Center-to-center cone spacing, $S(x,y)$, was calculated from density by assuming that cones are arranged in a perfect hexagonal lattice leading to an exact relationship between cone density and spacing:

$$S(x,y) = \left[\frac{2}{\sqrt{3}d(x,y)}\right]^{1/2} \quad (5)$$

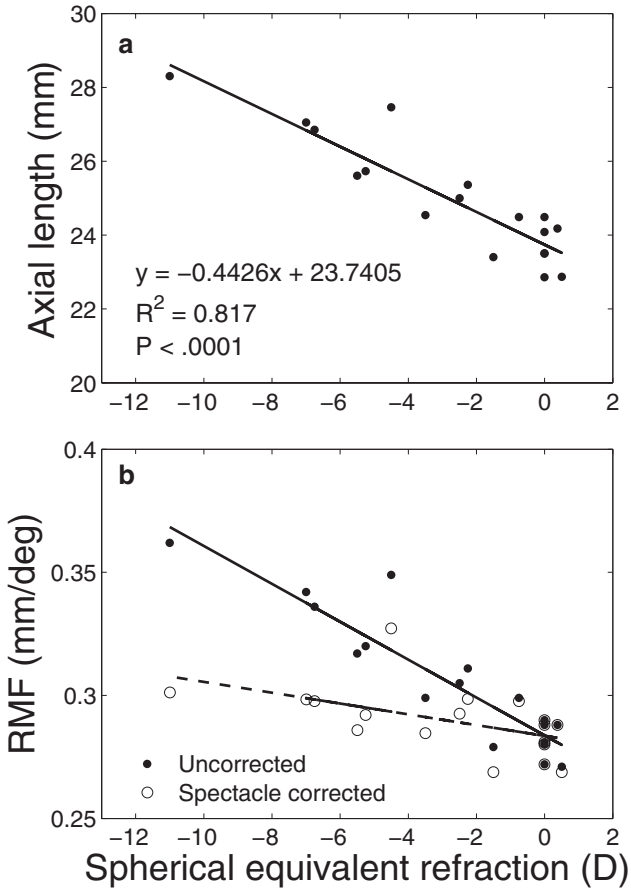

FIGURE 2. (**a**) Axial length plotted as a function of the spherical equivalent spectacle refraction with the *solid line* being a linear regression of the data. (**b**) Calculated RMF plotted as a function of the spherical equivalent spectacle refraction. Equation 2 was used directly to compute RMF for the uncorrected case, whereas the spectacle corrected RMFs were obtained by multiplying the uncorrected RMFs by the corresponding spectacle magnifications calculated with equation 3. Lines represent linear regressions of the data. The decrease in RMF with less refractive error was significant ($P < 0.05$) for both the corrected and uncorrected cases.

RESULTS

Axial length and RMF are plotted against spherical equivalent refraction in Figure 2, confirming once more that refractive error is primarily due to changes in axial length. Furthermore, the trend observed for both the corrected and uncorrected RMFs, in relation to the refractive error, are in close agreement with those reported in Coletta and Watson.[2] Stable AO performance, even in the cases without cycloplegia, was achieved without buildup of unobservable, deformable mirror modes (i.e., local waffling[36]) based on image intensity and residual wavefront error calculated from Shack-Hartmann images.[52] A low computed wavefront error did not always correspond to similar quality images, as we successfully resolved the entire foveal cone mosaic in only four eyes. Figure 3 shows an example of such an image covering approximately 2° across the foveal center. In the other subjects, the hexagonal packing structure of the cone mosaic gradually faded toward the foveal center, forming a region with an undesired, specklelike appearance. This region extended to at most 0.03 mm eccentricity for the majority of the eyes imaged, but went out as far as 0.10 mm eccentricity for one individual.

Foveal Fixation and Cone Density Topography

The PRL was determined from a series of fixation events and was analyzed in much the same way as described in Putnam et al.,[28] with the exception that the principal components of each set of fixation points were first computed to estimate the orientation of the distribution. In some cases, the principal components (semimajor and semiminor axes) were nearly parallel to the coordinate axes (Fig. 3), but a distribution such as the one shown in Figure 4 is more accurately described by a Gaussian function that is rotated by 143°. The standard deviation of fixation along the semimajor axis varied from 1.75 to 5.42 arc min (7.89–29.81 μm), with the mean at 3.61 arc min (18.74 μm). Fixation along the semiminor axis had a significantly lower standard deviation ($P < 0.01$), ranging from only 1.19 to 3.88 arc min (5.72–20.47 μm) and indicating that the angular distribution of foveal fixation is generally not uniform. Both sets of standard deviations are listed in Table 2. Fixation points along both axes were verified to be normally distributed (Kolmogorov-Smirnov test, $P > 0.05$) in nearly all recordings, the exceptions being subjects 2 and 13 along the semiminor axes and subjects 1 and 16 along the semimajor axes.

Figure 5 displays several topographic maps with isodensity contour lines. PRLs and foveal centers are denoted by the white dots and x's respectively. Zero contour levels are regions where cones were not reliably identified or areas beyond the image support. Displacements between PRLs and foveal centers ranged from 2.98 μm (0.58 arc min) to 92.29 μm (18.55 arc min) with an average displacement of approximately 34

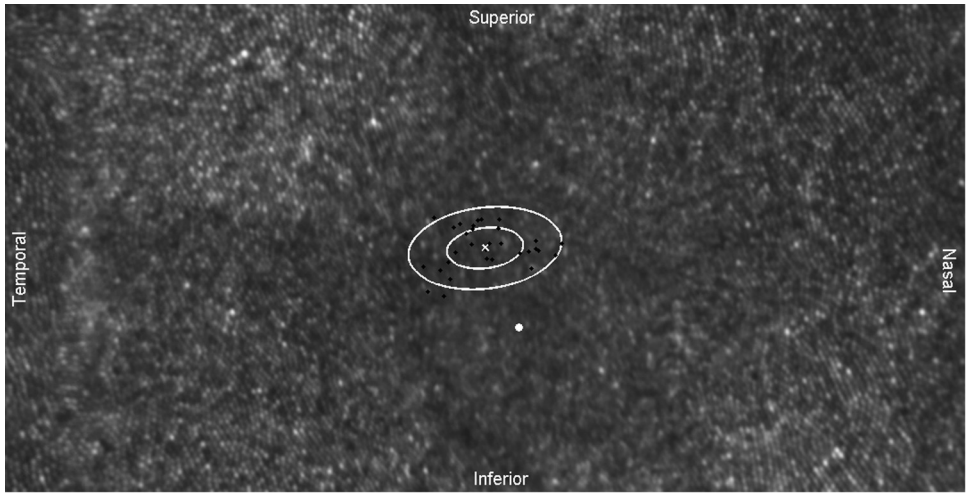

FIGURE 3. A 1° × 2° (320 × 640 μm) cone mosaic centered about the PRL (*white* x) for subject 13. *Black dots*: fixation locations; *white ellipses*: one and two standard deviations of the fixation points. The PRL is displaced approximately 9.5 arc min (50 μm) from the foveal center. (*white dot*).

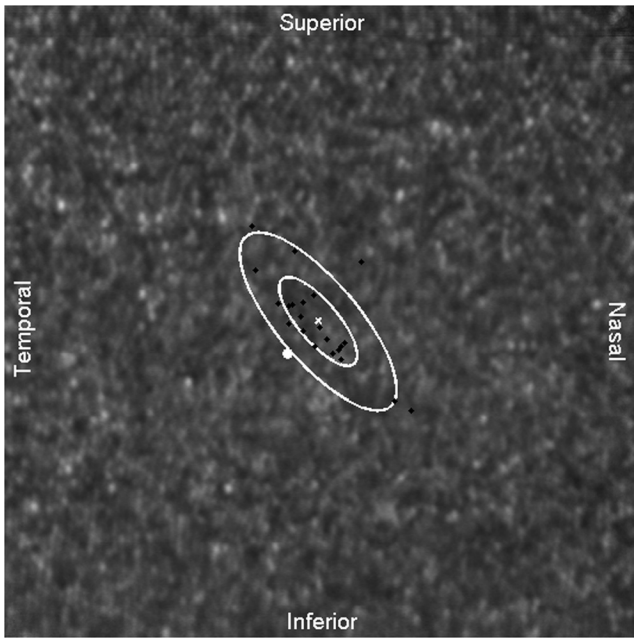

FIGURE 4. A 1° × 1° (336 × 336 μm) cone mosaic centered about the PRL (*white* x). *Small black dots*: fixation locations; *white dot*: location of the anatomic foveal center. The semimajor axis angle for the distribution of fixation is approximately 143°. The PRL is displaced approximately 3.9 arc min (22 μm) from the foveal center.

μm (5.62 arc min), which is lower on average than the estimates given by Putnam et al.,[28] measured with a flood illuminated AO ophthalmoscope. Table 2 lists the measured displacements in all subjects. A series of location tests on the PRLs, based on our estimates of the fixation variances, revealed that the PRL deviated significantly from the foveal center in all but one individual (*t*-test, two-tailed, $P < 0.001$). This finding can be qualitatively appreciated in Figure 5 by observing that the PRL generally deviated substantially from the center of mass of the corresponding contour map.

Cone Density Variability

Retinal cone density is plotted against retinal eccentricity in Figure 6, with 0 eccentricity defined at the foveal center. In the four eyes in which all the foveal cones were resolved, the peak retinal cone density ranged from 123,842 to 167,730 cones/mm^2 (Table 2), all of which fall within reported values, despite subtle differences in the calculation procedure used in different studies.[17,27,28] The corresponding minimum center-to-center cone spacing estimates were 2.62, 3.05, 2.77, and 2.79 μm. Individual cones were resolved in most eyes, beginning at ~0.03 mm eccentricity. On average, retinal cone density decreased from 151,008 to 57,312 cones/mm^2 from 0.03 to 0.30 mm eccentricity. Variability across subjects was highest at 0.03 mm eccentricity and converged to a similar range of values beyond 0.2 mm eccentricity.

In Figure 7, cone density is plotted against axial length at three different retinal eccentricities. At 0.10 mm eccentricity, retinal cone density appeared to decrease with increasing axial length, but the effect is not significant ($P > 0.05$). The root mean square error (RMSE) of 9114 cones/mm^2 is a clear indication that axial length does not accurately describe retinal cone density differences near the foveal center. By 0.30 mm eccentricity, however, retinal cone density decreased significantly with increasing axial length ($P < 0.05$), and the RMSE was reduced nearly threefold to only 4406 cones/mm^2. Since the RMF was higher in longer eyes, angular cone density increased significantly with axial length at all three retinal eccentricities, even though the RMSE of the fit was rather high toward the foveal center. As a result, the visual angle subtended by an object along the line of sight would generally be sampled by more cones in a longer eye, despite evidence of myopia-induced retinal stretching as close as 0.3 mm from the foveal center.

To facilitate comparisons between our anatomic measurements and visual acuity, we also analyzed the cone density data at specific angular eccentricities. Figure 8 shows that retinal cone density decreased with increasing axial length at a higher rate. However, retinal and angular eccentricities away from the foveal center have separate meanings when different eye sizes are involved. For example, 1° eccentricity converts to a dis-

TABLE 2. Peak Cone Density and Foveal Fixation

	Peak Density, cones/mm^2	Semimajor Axis Standard Deviation, arc min (μm)	Semiminor Axis Standard Deviation, arc min (μm)	Deviation of PRL from the Point of Peak Cone Density, arc min (μm)	
1	—	2.31 (10.5)	1.20 (5.4)	2.97 (13.5) N	6.94 (31.5) S
2	—	1.75 (7.9)	1.64 (7.4)	2.43 (11.0) T	1.78 (8.0) I
3	—	3.74 (17.4)	2.72 (12.6)	2.00 (9.3) N	7.51 (34.9) S
4	—	2.11 (9.9)	1.28 (6.0)	5.81 (27.2) N	6.08 (28.4) S
5	—	4.59 (21.5)	2.55 (12.0)	0.79 (3.7) T	5.62 (26.4) S
6	167,730	2.91 (14.0)	1.54 (7.4)	2.50 (12.0) T	1.62 (7.8) S
7	—	3.36 (16.2)	1.19 (5.7)	1.93 (9.3) N	7.96 (38.3) I
8	—	4.66 (23.2)	1.75 (8.7)	10.54 (52.5) T	15.26 (75.9) S
9	—	4.00 (19.9)	2.25 (11.2)	1.40 (7.0) N	6.51 (32.4) S
10	—	3.10 (15.5)	2.79 (13.9)	2.89 (14.4) T	1.98 (9.9) S
11	—	3.00 (15.3)	1.32 (6.7)	2.07 (10.5) N	0.94 (4.8) S
12*	—	3.42 (17.8)	1.63 (8.4)	0.54 (2.8) N	0.21 (1.1) S
13	116,217	5.42 (28.6)	3.88 (20.5)	2.73 (14.5) N	14.11 (74.5) S
14	167,984	4.83 (25.8)	2.51 (13.4)	3.16 (16.9) N	8.92 (47.6) S
15	149,719	5.33 (29.8)	1.95 (10.9)	2.71 (15.2) T	2.76 (15.4) S
16	—	2.85 (16.2)	2.65 (15.1)	5.07 (28.9) T	1.78 (10.1) S
17	—	4.35 (25.3)	2.38 (13.8)	0.90 (5.2) T	1.14 (6.6) S
18	—	3.19 (19.3)	2.23 (13.5)	1.62 (9.8) T	9.37 (56.6) S

Subjects are listed in the same order as in Table 1. Standard deviations are from Gaussian fits to each set of fixation locations. T, temporal; S, superior; N, nasal; I, inferior.

* PRL was not significantly different from the estimated foveal center.

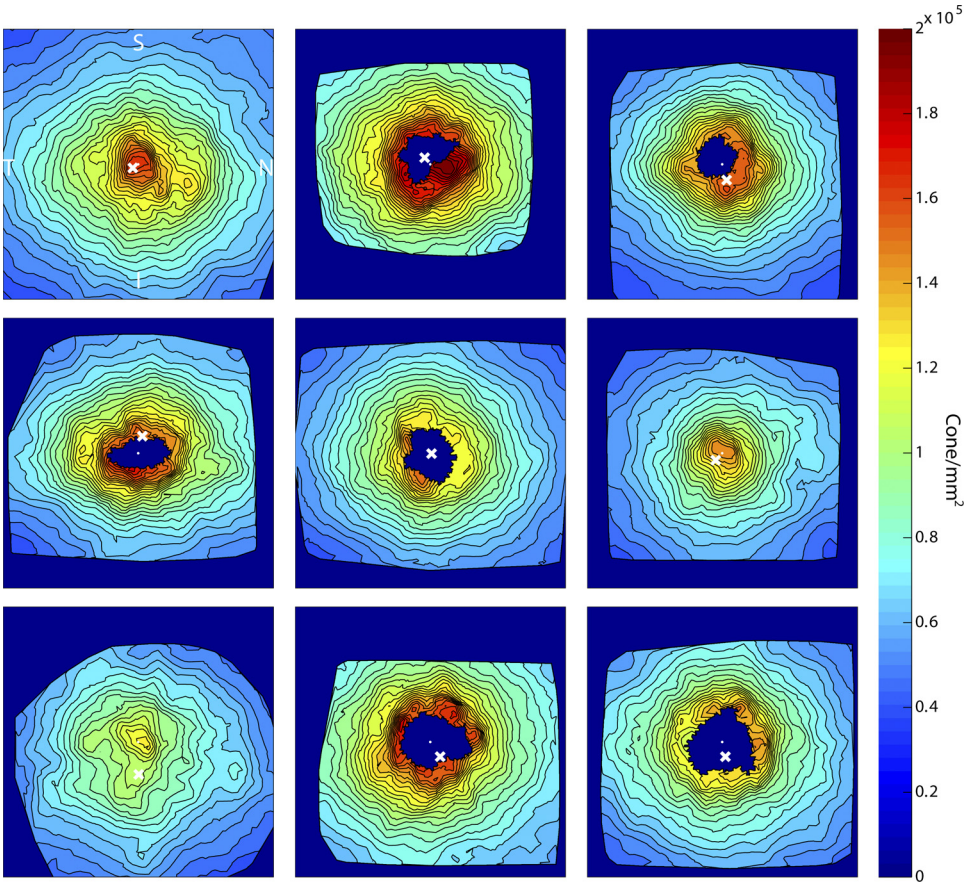

FIGURE 5. Examples of cone density topographic maps. All maps are oriented as indicated in the *top left* panel. T, temporal; S, superior; N, nasal; I, inferior. Locations of the foveal center and the PRL are indicated by a *white dot* and an x, respectively. The size of each map is 0.6 × 0.6 mm, and consecutive contour lines are separated by 5000 cones/mm^2. *Dark blue* areas include both the central foveal region in some eyes where cones could not be resolved and regions outside of the support of the acquired retinal images.

tance of 0.27 mm away from the foveal center for our shortest eye and more than 0.36 mm for our longest eye. According to our measurements, we would expect a cone density decrease of 14,785 cones/mm^2 owing to differences in retinal eccentricity alone, which explains approximately 52% of the estimated decrease in Figure 8c. The remaining 48% is presumably due to

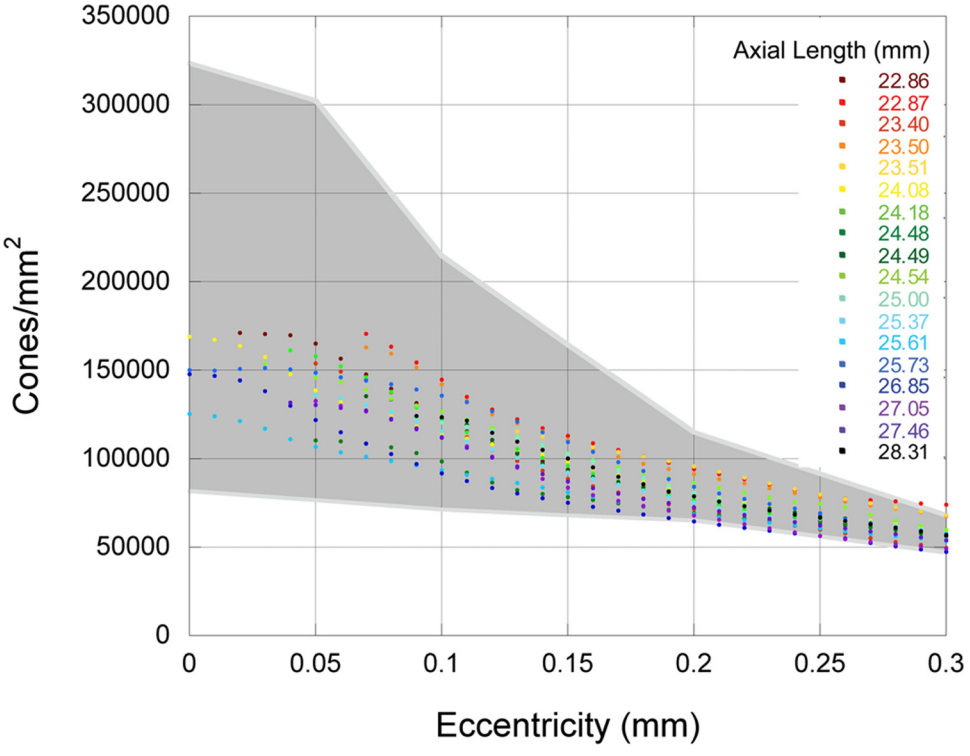

FIGURE 6. Retinal cone density as a function of retinal eccentricity. Representative cone density measurements at particular eccentricities were computed by circular averaging of density estimates around all meridians. The shaded region corresponds to the range of foveal cone density values reported by Curcio et al.[17]

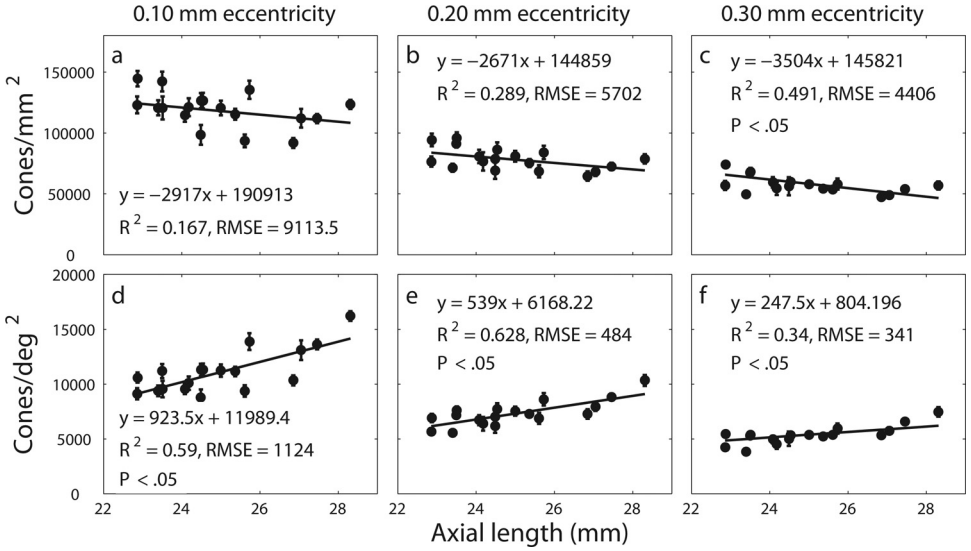

Figure 7. Retinal (**a–c**) and angular (**d–f**) cone density as a function of axial length at three different retinal eccentricities. Error bars represent one standard deviation in the spread of cone densities at the specified eccentricities. *Lines:* weighted least squares linear regression of the data.

retinal stretching. An increase in axial length did not seem to have any effect on angular cone density ($P > 0.05$). In fact, the regression line was nearly flat by 1° eccentricity, assuring that the visual angle subtended by an object that arrives slightly off axis will be sampled by a similar number of cones independent of axial length.

Since the PRL can deviate substantially from the foveal center, we were able to determine cone density at the PRL in 10 eyes, although some of the images contained a small region of cones that were not resolved. Figure 9 shows plots of the retinal cone density against axial length at the PRL. Retinal cone density appeared to decrease with increasing axial length, primarily due to a fairly long eye in our study that had particularly low cone densities at and near the foveal center, but the standard error was very high (RMSE = 22,154 cones/mm^2), and so the effect was still insignificant ($P > 0.05$).

Discussion

The lateral resolution of the AOSLO was sufficient for resolving the smallest foveal cones but not for all eyes, most likely because the amount of residual aberrations was subject dependent. One reason for the insufficient resolution is that the wavefront reconstructor in equation 1 was optimized for only a 6-mm diameter pupil. This size restriction poses a problem when imaging certain high myopes when the minifying effect of a high minus power lens is placed in front of the eye to bring the initial aberration magnitude to within a correctable range. In addition, the wavefront covariance matrix (**C**), used as a prior in optimizing the reconstructor, is designed to approximate a particular power spectrum.[53] AO performance depends on how well the aberration profile for a particular eye is approximated by this model. These limitations are currently being addressed by more accurate AO system modeling and control methods.[54–56]

In recent works, Chui et al.[3,57] stated that diffraction may be the limiting factor for the AOSLO for resolving cones near the foveal center. Their resolution assessment was based on the Rayleigh criterion for a 6 mm diameter pupil (2.8 μm for an emmetropic eye). For the subjects imaged in this study, the Rayleigh criterion would predict the resolution limit to be from 2.65 to 3.55 μm, depending on eye length. With the exception of the two high density foveas reported by Curcio et al.,[17] the smallest foveal cones are at least 2 μm in diameter which is approximately equal to cone spacing in the rod-free fovea.[17,48,58,59] Cone size increased rapidly with eccentricity, so

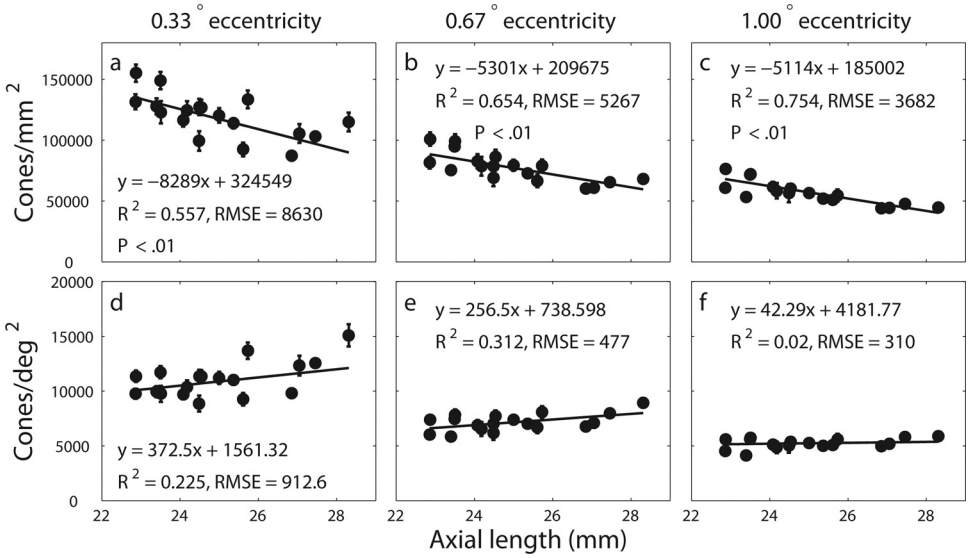

Figure 8. Retinal cone density (**a–c**) and angular cone density (**d–f**) as a function of axial length at three different angular eccentricities. Error bars represent one standard deviation in the spread of cone density values at the specified eccentricities. *Lines:* weighted least squares linear regression of the data.

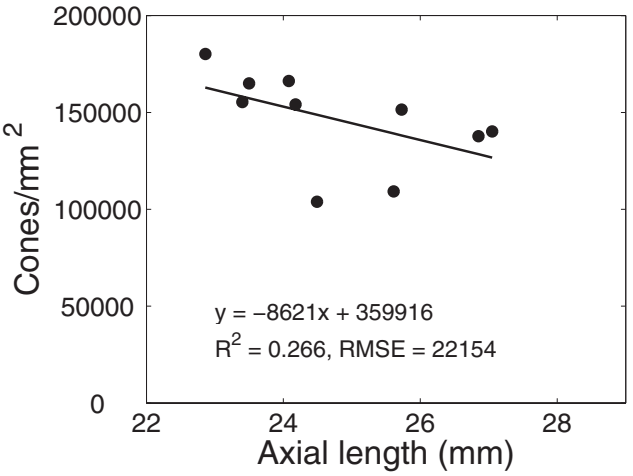

FIGURE 9. Retinal cone density as a function of axial length at the PRL. *Line*: linear regression of the data. The regression slope is insignificant ($P > 0.05$).

that by 150 μm away from the foveal center, the average cone spacing was greater than 3.5 μm, according to measurements plotted in Figure 6. Since Chui et al.[3,57] were able to resolve individual cones only at retinal eccentricities greater than 200 μm in emmetropes, it is unlikely that diffraction was the limiting factor. Fundamentally, the more accurate description of the resolution limit is the Sparrow criterion, which predicts a resolving power that is approximately 22% higher than the Rayleigh criterion for a circular aperture.[60–62] In this study, the predicted lateral resolutions in the four eyes were 2.41, 2.43, and 2.55 μm, indicating that we were imaging close to the diffraction limit. Assuming that size is the only factor that makes foveal cones difficult to image, a diffraction limited AOSLO should be able to resolve the entire foveal cone mosaic in most eyes. Because this was not the case in the present study, a more robust AO system is needed to consistently achieve near diffraction limited image quality.

In measuring fixation, the AOSLO has the advantage over other modalities for being able to isolate precise locations on the retina used for fixation. Any potential alignment or timing error is eliminated, because the fixation target is generated as part of the image formation process.[38] Nevertheless, our data are consistent with, albeit slightly lower than, those of Putnam et al.,[28] who found that the PRL is displaced from the point of peak cone density. Our measurements serve to confirm that the PRL deviates significantly from the foveal center and reinforces the importance of clearly defining the location of 0 eccentricity whenever one is performing eccentricity-dependent measurements. Furthermore, when the angular distribution of foveal fixation is not approximately uniform, the horizontal and vertical standard deviation or the mean would not accurately describe fixation variability. Principal component analysis determines the orientation that accounts for the most variability in the data and thus provides a better overall metric for describing fixation variability.

One of the main purposes of this work was to provide baseline cone density measurements from 0 to 0.3 mm eccentricity, a region of the retina that is most important for spatial vision, but that has been rarely explored using in vivo imaging methods. With improved AO performance, most if not all cone photoreceptors in this central part of the fovea can be resolved. The cone density curves plotted in Figure 6 are in close agreement with six of the eight retinas presented in Curcio et al.[17] It was mentioned as a possibility by the investigators that the two retinas with much higher foveal cone density than the rest may have been due to tissue shrinkage. It is nonetheless encouraging to find that in vivo density measurements are in close agreement with histologic data.

Inside the approximate foveola (0–0.2 mm eccentricity[17,63]), the axial length induced retinal stretching could not be verified by cone density measurements alone because of high levels of intersubject variability. Although we were able to measure cone density only as close as 0.1 mm eccentricity if all subjects were to be included, we would expect intersubject variability to be even greater at the foveal center on the basis of histologic data.[48] However, with increasing retinal eccentricity, the tendency for all cone mosaics to converge to a state that can be characterized by axial length becomes more apparent as observed at 0.3 mm eccentricity (Fig. 7c). Of interest, despite the amount of intersubject variability present near the foveal center, angular cone density actually increased significantly with axial length at any particular retinal eccentricity (Figs. 7d–f). In the interferometric acuity study conducted by Coletta and Watson,[2] the investigators generated a 1° diameter circular grating patch to measure foveal acuity in a group of subjects with various axial lengths. According to their results, all the subjects performed similarly when acuity limits were specified in angular units of spatial frequency (cycles/deg). On the basis of the RMF estimates, the spatial frequency of the grating in retinal units (cycles/mm) for the longest eye would be at about half the rate of that for the shortest eye. On the basis of our measurements, if interferometric acuity at the fovea is indeed limited by cone spacing, then one would expect individuals with longer eyes to perform better than those with shorter eyes in terms of acuity in angular units (cycles/deg) and to perform similarly in terms of acuity in retinal units (cycles/mm). Since this was not the case according to two separate studies,[2,23] we can rule out retinal stretching as a possible explanation for why foveal interferometric acuity does not improve with increasing level of axial myopia.

A rather extreme interpretation of our results is that the density of the foveolar cone mosaic is completely unaffected by myopia-related eye growth. This notion seems unlikely, because the retinal surface expands globally in myopia,[64] and we have little reason to believe that retinal tissue at the foveola is somehow more durable than that in the rest of the retina. A more reasonable interpretation would be that retinal stretching affects the foveolar cone mosaic, but a number of other developmental factors primarily govern cone density distribution there. A thorough analysis of foveal cone density and packing structure in emmetropic retinas, in tandem with other structural measures (i.e., retinal thickness, size of the foveal avascular zone, and shape of the foveal depression[65]) would be necessary to identify these potential factors. Nevertheless, since we were able to estimate the peak cone density in only four eyes, we still cannot rule out the possibility that peak cone density increases with eye growth, as seen in experimentally enlarged marmoset eyes.[16]

CONCLUSIONS

The lateral resolution achieved with AOSLO is sufficient for resolving the smallest cones in the foveola in some eyes and most of the foveal cones in all normal eyes. As a result, we were able to perform some of the first analyses of images of foveal cone mosaics acquired from the living human retina. AOSLO measurements of foveal fixation verified that the PRL deviates significantly from the point of peak cone density in normal eyes. On the basis of cone density distribution alone, myopia induced retinal stretching occurs in the fovea, but near the foveal center (<0.3 mm), these dependencies are confounded by other sources of intersubject variability. As a result, relation-

ships between cone density and axial length found outside this region cannot be extrapolated to infer trends at the foveal center or along the line of sight.

Acknowledgments

The authors thank Christine Wildsoet for insightful conversations regarding myopia, Scott Stevenson for providing excellent image stabilization software, Yuhua Zhang for constructing the AOSLO, and Michael Liu for assistance with image processing.

References

1. Chui TYP, Yap MKH, Chan HHL, Thibos LN. Retinal stretching limits peripheral visual acuity in myopia. *Vision Res.* 2005;45:593–605.
2. Coletta NJ, Watson T. Effect of myopia on visual acuity measured with laser interference fringes. *Vision Res.* 2006;46:636–651.
3. Chui TYP, Song H, Burns SA. Individual variations in human cone photoreceptor packing density: variations with refractive error. *Invest Ophthalmol Vis Sci.* 2008;49:4679–4687.
4. Strang NC, Winn B, Bradley A. The role of neural and optical factors in limiting visual resolution in myopia. *Vision Res.* 1998;38:1713–1721.
5. Bullimore MA, Gilmartin B, Royston JM. Steady-state accommodation and ocular biometry in late-onset myopia. *Doc Ophthalmol.* 1992;80:143–155.
6. Lam AKC, Wong S, Lam CSY, To CH. The effect of myopic axial elongation and posture on the pulsatile ocular blood flow in young normal subjects. *Optom Vision Sci.* 2002;79:300–305.
7. Kitaguchi Y, Bessho K, Yamaguchi T, Nakazawa N, Mihashi T, Fujikado T. In vivo measurements of cone photoreceptor spacing in myopic eyes from images obtained by an adaptive optics fundus camera. *Jpn J Ophthalmol.* 2007;51:456–461.
8. Adams AJ. Axial length elongation, not corneal curvature, as a basis of adult onset myopia. *Am J Optom Physiol Opt.* 1987;64:150–152.
9. Mcbrien NA, Millodot M. A biometric investigation of late onset myopic eyes. *Acta Ophthalmol.* 1987;65:461–468.
10. Rossi EA, Weiser P, Tarrant J, Roorda A. Visual performance in emmetropia and low myopia after correction of high-order aberrations. *J Vis.* 2007;7:14.
11. Liou SW, Chiu CJ. Myopia and contrast sensitivity function. *Curr Eye Res.* 2001;22:81–84.
12. Jaworski A, Gentle A, Zele AJ, Vingrys AJ, McBrien NA. Altered visual sensitivity in axial high myopia: a local postreceptoral phenomenon? *Invest Ophthalmol Vis Sci.* 2006;47:3695–3702.
13. Abbott ML, Schmid KL, Strang NC. Differences in the accommodation stimulus response curves of adult myopes and emmetropes. *Ophthalmic Physiol Opt.* 1998;18:13–20.
14. O'Leary DJ, Allen PM. Facility of accommodation in myopia. *Ophthalmic Physiol Opt.* 2001;21:352–355.
15. Vera-Diaz FA, McGraw PV, Strang NC, Whitaker D. A psychophysical investigation of ocular expansion in human eyes. *Invest Ophthalmol Vis Sci.* 2005;46:758–763.
16. Troilo D. Changes in retinal morphology following experimentally induced myopia. Vol 1. *Technical Digest Series*: *Vision Science and Its Application.* Washington, DC: Optical Society of America; 1998;1:206–209.
17. Curcio CA, Sloan KR, Kalina RE, Hendrickson AE. Human photoreceptor topography. *J Comp Neurol.* 1990;292:497–523.
18. Williams DR. Topography of the foveal cone mosaic in the living human-eye. *Vision Res.* 1988;28:433–454.
19. Marcos S, Tornow RP, Elsner AE, Navarro R. Foveal cone spacing and cone photopigment density difference: objective measurements in the same subjects. *Vision Res.* 1997;37:1909–1915.
20. Marcos S, Burns SA. Cone spacing and waveguide properties from cone directionality measurements. *J Opt Soc Am A Opt Image Sci Vis.* 1999;16:995–1004.
21. Atchison DA, Jones CE, Schmid KL, et al. Eye shape in emmetropia and myopia. *Invest Ophthalmol Vis Sci.* 2004;45:3380–3386.
22. Bradley A, Hook J, Haeseker J. A comparison of clinical acuity and contrast sensitivity charts: effect of uncorrected myopia. *Ophthalmic Physiol Opt.* 1991;11:218–226.
23. Atchison DA, Schmid KL, Pritchard N. Neural and optical limits to visual performance in myopia. *Vision Res.* 2006;46:3707–3722.
24. Mujat M, Ferguson RD, Iftimia N, Hammer DX. Compact adaptive optics line scanning ophthalmoscope. *Opt Express.* 2009;17:10242–10258.
25. Liang JZ, Williams DR, Miller DT. Supernormal vision and high-resolution retinal imaging through adaptive optics. *J Opt Soc Am A.* 1997;14:2884–2892.
26. Roorda A, Romero-Borja F, Donnelly WJ, Queener H, Hebert TJ, Campbell MCW. Adaptive optics scanning laser ophthalmoscopy. *Opt Express.* 2002;10:405–412.
27. Carroll J, Neitz M, Hofer H, Neitz J, Williams DR. Functional photoreceptor loss revealed with adaptive optics: an alternate cause of color blindness. *Proc Natl Acad Sci U S A.* 2004;101:8461–8466.
28. Putnam NM, Hofer HJ, Doble N, Chen L, Carroll J, Williams DR. The locus of fixation and the foveal cone mosaic. *J Vis.* 2005;5:632–639.
29. Zhang Y, Poonja S, Roorda A. MEMS-based adaptive optics scanning laser ophthalmoscopy. *Opt Lett.* 2006;31:1268–1270.
30. Zhang Y, Poonja S, Roorda A. AOSLO: from benchtop to clinic. *Proc SPIE.* 2006;6306:63060V.
31. Law NF, Lang RG. Wavefront estimation at low light levels. *Opt Commun.* 1996;126:19–24.
32. Li KY, Mishra S, Tiruveedhula P, Roorda A. Comparison of control algorithms for a MEMS-based adaptive optics scanning laser ophthalmoscope. *Proceedings of the 2009 American Control Conference.* 2009;3848–3853.
33. Boyer C, Michau V, Rousset G. Adaptive optics: interaction matrix measurement and real-time control algorithms for the come-on project. *Proc SPIE.* 1990;1542:46–61.
34. Jiang W, Li H. Hartmann-Shack wave-front sensing and wave-front control algorithm. *Proc SPIE.* 1990;1271:82–93.
35. van Dam MA, Bouchez AH, Le Mignant D, et al. The W M Keck Observatory laser guide star adaptive optics system: performance characterization. *Publication of the Astronomical Society of the Pacific.* 2006;118:310–318.
36. Gavel D. Suppressing anomalous localized waffle behavior in least squares wavefront reconstructors. *Proc SPIE.* 2002;4839:972–980.
37. van Dam MA, Le Mignant D, Macintosh BA. Performance of the Keck Observatory adaptive-optics system. *Appl Opt.* 2004;43:5458–5467.
38. Poonja S, Patel S, Henry L, Roorda A. Dynamic visual stimulus presentation in an adaptive optics scanning laser ophthalmoscope. *J Refract Surg.* 2005;21:S575–S580.
39. Arathorn DW, Yang Q, Vogel CR, Zhang Y, Tiruveedhula P, Roorda A. Retinally stabilized cone-targeted stimulus delivery. *Opt Express.* 2007;15:13731–13744.
40. Stevenson SB, Roorda A. Correcting for miniature eye movements in high resolution scanning laser ophthalmoscopy. *Proc SPIE.* 2005:5688:145–151.
41. Li KY, Roorda A. Automated identification of cone photoreceptors in adaptive optics retinal images. *J Opt Soc Am A Opt Image Sci Vis.* 2007;24:1358–1363.
42. Bennett AG, Rudnicka AR, Edgar DF. Improvements on Littmann method of determining the size of retinal features by fundus photography. *Graefes Arch Clin Exp Ophthalmol.* 1994;232:361–367.
43. Martin JA, Roorda A. Pulsatility of parafoveal capillary leukocytes. *Exp Eye Res.* 2009;88:356–360.
44. Doughty MJ, Zaman ML. Human corneal thickness and its impact on intraocular pressure measures: a review and meta-analysis approach. *Surv Ophthalmol.* 2000;44:367–408.
45. Patel S, Marshall J, Fitzke FW. Refractive-index of the human corneal epithelium and stroma. *J Refract Surg.* 1995;11:100–105.
46. Williams TD. Determination of the true size of an object on the fundus of the living eye. *Optom Vis Sci.* 1992;69:717–720.
47. Hecht E. Analytical ray tracing. In: Black A, ed. *Optics.* Reading, MA: Addison Wesley Longman, Inc.; 2002:246–253.

48. Curcio CA, Sloan KR. Packing geometry of human cone photoreceptors: variation with eccentricity and evidence for local anisotropy. *Vis Neurosci.* 1992;9:169–180.
49. Breu H, Gil J, Kirkpatrick D, Werman M. Linear-Time Euclidean distance transform algorithms. *IEEE Trans Pattern Anal Mach Intell.* 1995;17:529–533.
50. Costa LD, Rocha F, de Lima SMA. Characterizing polygonality in biological structures. *Phys Rev E.* 2006;73:1–8.
51. Costa LD, Bonci DMO, Saito CA, Rocha FAD, Silveira LCD, Ventura DF. Voronoi analysis uncovers relationship between mosaics of normally placed and displaced amacrine cells in the thraira retina. *Neuroinformatics.* 2007;5:59–77.
52. Herrmann J. Least-squares wave-front errors of minimum norm. *J Opt Soc Am A.* 1980;70:28–35.
53. Cagigal MP, Canales VF, Castejon-Mochon JF, Prieto PM, Lopez-Gil N, Artal P. Statistical description of wave-front aberration in the human eye. *Opt Lett.* 2002;27:37–39.
54. Vogel CR, Yang Q. Modeling, simulation, and open-loop control of a continuous facesheet MEMS deformable mirror. *J Opt Soc Am A.* 2006;23:1074–1081.
55. Ellerbroek BL. Efficient computation of minimum-variance wave-front reconstructors with sparse matrix techniques. *J Opt Soc Am A.* 2002;19:1803–1816.
56. Stewart JB, Diouf A, Zhou YP, Bifano TG. Open-loop control of a MEMS deformable mirror for large-amplitude wavefront control. *J Opt Soc Am A Opt Image Sci Vis.* 2007;24:3827–3833.
57. Chui TYP, Song HX, Burns SA. Adaptive-optics imaging of human cone photoreceptor distribution. *J Opt Soc Am A Opt Image Sci Vis.* 2008;25:3021–3029.
58. Yuodelis C, Hendrickson A. A qualitative and quantitative: analysis of the human fovea during development. *Vision Res.* 1986;26:847–855.
59. Obrien B. Vision and resolution in the central retina. *J Opt Soc Am.* 1951;41:882–894.
60. Sparrow CM. On spectroscopic resolving power. *Astrophys J.* 1916;44:76–86.
61. Grimes DN, Thompson BJ. 2-Point resolution with partially coherent light. *J Opt Soc Am.* 1967;57:1330–1334.
62. Hecht E. Fraunhofer diffraction. In: Black A, ed. *Optics.* Reading, MA: Addison Wesley Longman, Inc.; 2002:452–485.
63. Polyak S. Retinal structure and colour vision. *Doc Ophthalmol.* 1949;3:24–56.
64. Atchison DA, Pritchard N, Schmid KL, Scott DH, Jones CE, Pope JM. Shape of the retinal surface in emmetropia and myopia. *Invest Ophthalmol Vis Sci.* 2005;46:2698–2707.
65. Dubis AM, McAllister JT, Carroll J. Reconstructing foveal pit morphology from optical coherence tomography imaging. *Br J Ophthalmol.* 2009;93:1223–1227.